J. Fluid Mech. (2009), *vol.* 626, *pp.* 367–393.
doi:10.1017/S0022112009006442 Printed in the United Kingdom

Numerical study of electric field effects on the deformation of two-dimensional liquid drops in simple shear flow at arbitrary Reynolds number

STEFAN MÄHLMANN[1] AND
DEMETRIOS T. PAPAGEORGIOU†[1,2]

[1]Department of Mathematical Sciences, New Jersey Institute of Technology, Newark, NJ 07102, USA
[2]Department of Mathematics, Imperial College London, London SW7 2AZ, UK

(Received 22 January 2008 and in revised 30 December 2008)

The effect of an electric field on a periodic array of two-dimensional liquid drops suspended in simple shear flow is studied numerically. The shear is produced by moving the parallel walls of the channel containing the fluids at equal speeds but in opposite directions and an electric field is generated by imposing a constant voltage difference across the channel walls. The level set method is adapted to electrohydrodynamics problems that include a background flow in order to compute the effects of permittivity and conductivity differences between the two phases on the dynamics and drop configurations. The electric field introduces additional interfacial stresses at the drop interface and we perform extensive computations to assess the combined effects of electric fields, surface tension and inertia. Our computations for perfect dielectric systems indicate that the electric field increases the drop deformation to generate elongated drops at steady state, and at the same time alters the drop orientation by increasing alignment with the vertical, which is the direction of the underlying electric field. These phenomena are observed for a range of values of Reynolds and capillary numbers. Computations using the leaky dielectric model also indicate that for certain combinations of electric properties the drop can undergo enhanced alignment with the vertical or the horizontal, as compared to perfect dielectric systems. For cases of enhanced elongation and alignment with the vertical, the flow positions the droplets closer to the channel walls where they cause larger wall shear stresses. We also establish that a sufficiently strong electric field can be used to destabilize the flow in the sense that steady-state droplets that can exist in its absence for a set of physical parameters, become increasingly and indefinitely elongated until additional mechanisms can lead to rupture. It is suggested that electric fields can be used to enhance such phenomena.

1. Introduction

The motion of liquid drops in a shear flow is a fundamental problem arising in several applications including emulsification, mixing and the rheology of suspensions. Important issues in these flows include the effect of parameters on the elongation and possible drop breakup as well as the resulting flow inside the drops which affects convective transport and mixing. Both of these phenomena are of relevance

† E-mail address for correspondence: d.papageorgiou@imperial.ac.uk

to microfluidic applications and lab-on-a-chip technologies that are receiving considerable attention (Stone, Stroock & Ajdari 2004; De Menech 2006; Song, Chen & Ismagilov 2006).

The present study formulates and studies computationally the dynamics of viscous two-dimensional drops subjected to a linear shear in a Couette device which is filled with a second immiscible viscous fluid. Inertia and surface tension forces are retained as has been done in previous two- and three-dimensional studies in the absence of electrostatic fields (Sheth & Pozrikidis 1995; Li, Renardy & Renardy 2000; Renardy & Cristini 2001; Khismatulin, Renardy & Cristini 2003; Wagner, Wilson & Cates 2003; Cristini & Tan 2004; Lee & Pozrikidis 2006). In the related studies of Sibillo *et al.* (2006) and Renardy (2007), the effect of confinement and inertia is considered in detail. It is reported that confinement in microchannels enables a drop to sustain significant elongation before breakup can occur, and the mechanism is deemed to promote a monodisperse droplet distribution.

An alternative method of producing monodisperse droplet distributions in microchannels is the use of electric fields. This has been demonstrated in the experiments of Ozen *et al.* (2006) at fairly small shear rates characterized by Reynolds numbers of order $\mathcal{O}(10^{-2})$. Ozen *et al.* produced highly stable two-fluid Poiseuille flows in microchannels and studied their stability under vertical electric fields. The field causes instability leading to an interfacial flapping motion that causes periodic collisions with the walls. As long as the electric field is acting, an array of alternating plugs of the two fluids emerge downstream and are carried along with the flow. When the field is switched off, the shapes relax to form a monodisperse array of droplets of one fluid suspended in the second fluid. Suspended drop volumes decrease with increasing electric fields; they can be relatively small and spherical or large and similar to a Bretherton bubble (Bretherton 1961). The reader is referred to Ozen *et al.* (2006) for experimental results and photographs of the phenomenon.

In applications, the separation of the two fluids can be used to perform reactions where mixing inside the droplets is essential (see for example the review by Song *et al.* 2006 and references therein). In the framework of the experiment of Ozen *et al.* described above, we envision a second stage where the electric field is imposed once again on the monodisperse train of droplets. The aim is to enhance mixing through a competition between viscous, electrical and surface tension stresses along with inertia. Ward & Homsy (2001, 2003) have demonstrated (theoretically and experimentally) that electric fields can be used to induce mixing in translating droplets. In order to obtain a fundamental understanding of the different mechanisms through a direct simulation, we choose a model problem of a periodic array of drops in a Couette device whose walls move at equal and opposite velocities U. In the absence of electric fields, this problem has been solved numerically in the Stokes and Navier–Stokes regimes. The present work is a systematic study of electric field effects on droplets immersed in a simple shear flow. The work of Fernández *et al.* (2005) on the effects of electrostatic forces on oblate drops in a channel is of relevance to the present calculations and is discussed in detail below.

There have been numerous studies on the effect of a simple shear on viscous two-dimensional drops suspended in a channel in the absence of electric fields. When inertia is absent calculations based on boundary integral equation methods have provided a fairly complete picture of the flow. It has been established by Kennedy, Pozrikidis & Skalak (1994) and Stone (1994) (see also Zhou & Pozrikidis 1993*a*, *b*, 1994; Li, Zhou & Pozrikidis 1995; Li, Charles & Pozrikidis 1996; Charles & Pozrikidis 1998), that if the drop is sufficiently more viscous than the suspending fluid then the

shear flow deforms it until it reaches an oblate stationary shape independent of the value of the surface tension. Elongation and indefinite thinning occurs in principle for large drop viscosities at zero Reynolds number as the shear is increased, but eventually the drop can break up due to non-hydrodynamic effects such as Van der Waals forces. Singular events such as cusp formation may take place in sheared two-dimensional interfacial flows as has been demonstrated by Pozrikidis (1997, 1998). In axisymmetric geometries the phenomena are quite distinct due to the presence of the Rayleigh instability that acts to break up an elongated axisymmetric droplet (Taylor 1934; Rallison & Acrivos 1978; Rallison 1981; Ryskin & Leal 1984). In such cases inertia acts to shift the critical value of the capillary number Ca (defined to be the ratio of viscous to capillary forces) where breakup occurs. For example a sufficiently large Reynolds number can induce breakup at capillary numbers where no breakup is observed at zero Reynolds number (Li *et al.* 2000; Renardy & Cristini 2001). By concentrating on two-dimensional droplets we aim to isolate the effects of inertia and electrostatic forces from three-dimensional destabilizations due to surface tension.

The computational study of Sheth & Pozrikidis (1995) uses a variant of the immersed boundary method (Peskin 1977). A periodic array of initially circular drops of different viscosities is introduced in a bounded Couette flow and the problem is evolved in time. The relevant parameters are the capillary number Ca, the Reynolds number Re, the drop to surrounding fluid viscosity ratio λ, the initial drop size and the separation between drops. Results are presented for fixed drop size and drop separation distance at Reynolds numbers $Re = 1, 10, 50, 100$, viscosity ratios $\lambda = 1, 10$ and a range of capillary numbers. The effect of inertia on steady-state deformed drops is to lead to more elongated steady states initially, and if Re is increased sufficiently an indefinite elongation emerges without a final steady state. A similar behaviour is found starting from a fixed Re and a sufficiently small value of Ca which is then increased – as the surface tension is reduced deformation is enhanced and no steady states emerge at sufficiently large Ca. The critical value of Ca (for flows of a given viscosity ratio λ), which separates steady states and indefinitely deformed ones, is found to decrease as the Reynolds number is increased. At values of λ that are sufficiently large so that if they are immersed in a Stokes flow they would reach a steady deformed state, it is found that as the Reynolds number is increased they can be caused to deform indefinitely, establishing that inertia is a mechanism that promotes drop deformation. Similar findings are reported by Wagner *et al.* (2003) who use lattice Boltzmann methods to perform their computations.

When electric fields are present the electrostatic forces act to modify the scenario described above. The purpose of the present work is a detailed study of such effects for pairs of dielectric and leaky dielectric fluids. The idealization to non-conducting perfect dielectric fluids is a useful leading-order approximation. If we allow the fluids to be poor conductors, then even a small conductivity allows electric charge carriers to reach the drop interface and form a diffuse charge layer there. In perfect dielectrics the normal components of the electric displacement field on either side of the interface match so that there is no such charge layer. In leaky dielectrics, charge accumulates at the interface to adjust the field and to ensure conservation of the electric current when the conductivities of the fluids differ. However, some cases have been reported where oblate shapes were observed while prolate deformations were predicted theoretically (O'Konski & Thacher 1953; Allan & Mason 1962). Taylor (1966) noticed that equilibrium shapes in leaky dielectrics only exist if the electric stresses are balanced by variable pressure differences across the interface. This implies in turn, that at equilibrium the fluids inside and outside the drop are in

continuous motion, even if the incident flow is zero. In the same paper Taylor analysed the static configuration of spherical drops in the zero Reynolds number limit and derived analytically a relation that discriminates between prolate and oblate forms. For more recent work on the electrohydrodynamics of drops including axisymmetric configurations we refer the reader to Feng & Scott (1996), Feng (1999, 2002), Lac & Homsy (2007), Collins *et al.* (2008) and references therein.

In a recent study, Fernández *et al.* (2005) consider electrostatic effects on two-dimensional oblate drops in a channel. They consider low conductivity cases and use the leaky dielectric model (see Smith & Melcher 1967; Melcher & Taylor 1969; Saville 1997). Using the front tracking algorithm of Unverdi & Tryggvason (1992), they compute the electrohydrodynamic flow at finite Reynolds numbers for a large number of drops that model an emulsion. The parameters are chosen so that the drops remain almost spherical and attention is focused on the formation of chains of drops that align with the electric field and can span the channel, at least for low flow rates. It is shown that the parameters can be chosen so that the flow can induce an attraction of drops which are in line with the electric field but a repulsion of drops which are in a line perpendicular to the field. For low flow rates the drops can form chains or fibres which span the channel; these chains are broken up at higher flow rates and short fibres are found on the walls, while at even higher flow rates the shear prevents chain formation and a suspension of drops emerges. In this study, we are mostly interested in drop sizes that are much larger than those of Fernández *et al.* (2005) which can undergo significant deformation; this is motivated by the experiments of Ozen *et al.* (2006). In their mathematical model, Fernández *et al.* (2005) approximated the discontinuous jump in the electric permittivity across the interface by a smoothed function. Then, by assuming that the electric field and the dielectric permittivity are continuous they incorporated a reduced form of the electrohydrodynamic force into the momentum equations (Saville 1997). Note that the proper form of the electrohydrodynamic force for methods that utilize smoothing is still an open question. More recently, Tomar *et al.* (2007) derived a new representation of the electrohydrodynamic force that satisfies the concept of continuum forces introduced by Brackbill, Kothe & Zamech (1992). In the same publication, they presented validation results of their model for a set of test problems with exact or approximate solutions in the absence of a background shear flow. The present study involves a background shear and as a result there is little overlap with the work of Tomar *et al.* (2007).

The remainder of the paper is organized as follows: In § 2 the mathematical model is formulated. The method of solution is described in § 3. This leads to § 4, where the results of our computations for a wide range of parameters are given. Finally, § 5 is devoted to concluding remarks.

2. Formulation and governing equations

In this section we summarize the mathematical model that is employed to study the effects of an electric field on a periodic array of liquid drops in simple shear flow. The hydrodynamics are governed by the incompressible Navier–Stokes equations and the electrostatic model is used to describe electric field effects. Since material and electrical properties are taken to be constant in each phase, the electromechanical coupling occurs at the interface that separates the drop phase and the suspending fluid. We refer the reader to the comprehensive reviews on electrohydrodynamics by

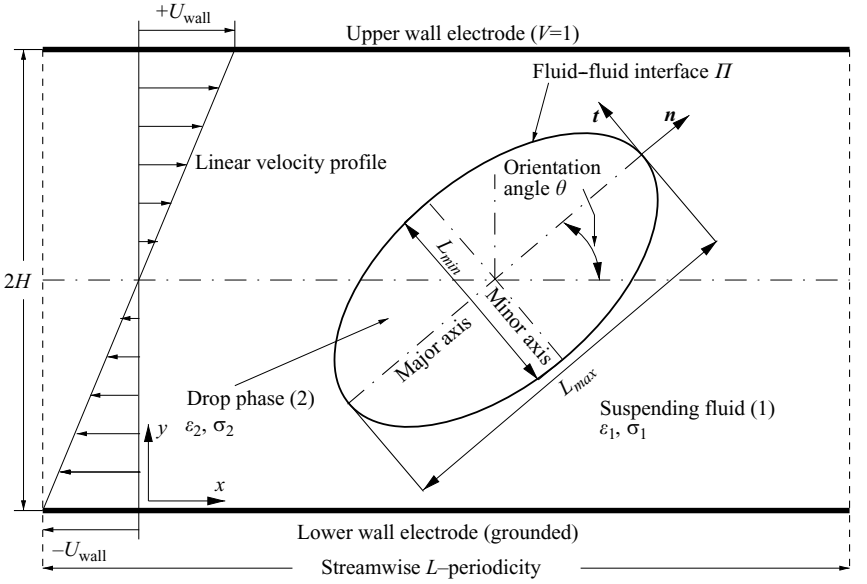

FIGURE 1. Schematic illustration of a periodic array of liquid drops in a Couette device when an vertical electric field is present in the gap.

Melcher & Taylor (1969) and Saville (1997) (see also Smith & Melcher 1967 for a detailed discussion of the mathematical model).

Figure 1 shows a schematic illustration of one period of an infinite array of liquid drops in a Couette flow device when a vertical electric field is present in the gap between the walls. The drop phase and the surrounding fluid are immiscible and can have different material properties. Here, Ω_1 and Ω_2 represent the regions occupied by the suspending fluid and the drop phase, respectively. The two regions are separated by a deformable interface Π, which can in general represent discontinuities in pressure, density, dielectric permittivity, conductivity and viscosity. The fluid flow in the two regions combined with the motion of the interface constitute a nonlinear time-dependent problem. The flows in each region are governed by the conservation equations for mass and momentum

$$\nabla \cdot \boldsymbol{u}_i = 0, \tag{2.1}$$

$$\rho_i \frac{\mathrm{D}\boldsymbol{u}_i}{\mathrm{D}t} = -\nabla p_i + \nabla \cdot (\mu_i 2\mathscr{D}_i), \tag{2.2}$$

where $\mathscr{D}_i := (1/2)(\nabla \boldsymbol{u} + \nabla \boldsymbol{u}^{\mathrm{T}})$ is the rate of deformation tensor, $\mathrm{D}/\mathrm{D}t = \partial_t + (\boldsymbol{u} \cdot \nabla)$ is the Lagrangian time derivative, $\boldsymbol{u}$ is the velocity vector, p is the pressure, ρ is the density and μ is the dynamic viscosity. The boundary conditions are those of no slip (implying no penetration also) at the rigid channel walls and periodicity in the horizontal direction – the boundary conditions at the drop surface are given below. Buoyancy has been neglected in the momentum equations (2.2). Furthermore, we set $\rho_1/\rho_2 = \mu_1/\mu_2 = 1$. Although a parametric study of the effects of varying ρ_1/ρ_2 and μ_1/μ_2 would be interesting, here we only present results for varying Reynolds number, capillary number and electric Weber number. To characterize the electric properties of the two-fluid suspension, we introduce the ratio of the dielectric permittivities $S^{-1} = \epsilon_2/\epsilon_1$ and the ratio of the conductivities $R = \sigma_2/\sigma_1$, where the subscripts 1 and 2 refer to the drop phase and the suspending fluid, respectively (note that our notation

follows that of Taylor 1966). Since the interface is massless, the forces in the fluids on the two sides of the interface must balance. The corresponding force balances in the normal and tangential directions at the interface in the presence of an applied electric field read

$$\left.\begin{aligned} \Gamma\gamma + ||\boldsymbol{n}\cdot T\cdot\boldsymbol{n}|| &= 0 \\ ||\boldsymbol{n}\cdot T\cdot\boldsymbol{t}|| &= 0 \end{aligned}\right\} \quad \text{on} \quad \Pi, \tag{2.3}$$

where T denotes the tensor containing both viscous and electrical contributions, γ is the curvature of the interface, Γ is the constant surface tension coefficient and $\boldsymbol{n}$ and $\boldsymbol{t}$ are unit normal (outward pointing from the drop phase) and unit tangent vectors, respectively. Furthermore, in viscous flows the velocities must be continuous across the interface, i.e. $||v||=0$. The jump notation $||\mathscr{G}||=\mathscr{G}_2-\mathscr{G}_1$ has also been introduced. The electrohydrodynamic coupling through the interfacial conditions (2.3) is accomplished by application of the continuum surface force (CSF) method (Brackbill *et al.* 1992; Unverdi & Tryggvason 1992). This is achieved by converting the sharp interface condition (2.3-1) into a volume integral that is implicitly incorporated into the momentum equations as a volumetric source term. Furthermore, by assuming that the material properties in the neighbourhood of the interface are solely functions of a scalar quantity ϕ, we obtain the one-fluid formulation

$$\rho\frac{\mathrm{D}\boldsymbol{u}}{\mathrm{D}t} = -\nabla p + \mu\nabla\cdot 2\mathscr{D} - \Gamma\gamma(\phi)\delta(\phi)\nabla\phi + \boldsymbol{F}^{el}, \tag{2.4}$$

where $\boldsymbol{F}^{el}$ is the contribution due to the electric field (see (2.8)), and $\delta(\phi)$ is the one-dimensional Dirac δ-function. Since discontinuous jumps of the material properties $\boldsymbol{q}(\phi)=\{\epsilon,\sigma\}(\phi)$ across the interface may introduce spurious oscillations in the numerical solutions, we approximate these quantities in a neighbourhood θ of the interface by

$$\boldsymbol{q}^{\theta} = \boldsymbol{q}_2 + (\boldsymbol{q}_1-\boldsymbol{q}_2)\mathscr{H}^{\theta}(\phi), \tag{2.5}$$

where $\mathscr{H}^{\theta}$ denotes the smoothed Heaviside function

$$\mathscr{H}^{\theta}(\phi) := \begin{cases} 0 & \text{if } \phi<-\theta \\ \frac{1}{2}\left(1+\frac{\phi}{\theta}+\frac{1}{\pi}\sin\left(\frac{\pi\phi}{\theta}\right)\right) & \text{if } |\phi|\leqslant\theta \\ 1 & \text{if } \phi>0. \end{cases} \tag{2.6}$$

In the computations reported here we set the thickness of the transition region $\theta=1.5h$, where h denotes the distance between two adjacent mesh nodes. Similarly, the δ-function in (2.4) is replaced by its smoothed version

$$\delta^{\theta}(\phi)=\frac{\mathrm{d}\mathscr{H}^{\theta}(\phi)}{\mathrm{d}\phi} = \begin{cases} \frac{1}{2\theta}\left(1+\cos\left(\frac{\pi\phi}{\theta}\right)\right) & \text{if } |\phi|<\theta \\ 0 & \text{elsewhere.} \end{cases} \tag{2.7}$$

The new force term on the right-hand side of the momentum equations (2.4) is the electric force density $\boldsymbol{F}^{el}$ which originates from the discontinuity of the electric stresses across the interface. The non-zero net electric stresses arise due to a mismatch of the electric displacement vector $\boldsymbol{D}=\epsilon\epsilon_0\boldsymbol{E}$ in the direction perpendicular to the interface, i.e. $\boldsymbol{n}\cdot|\boldsymbol{D}|=q_s$, where ϵ_0 is the permittivity of free space ($\epsilon_0=8.85\times10^{-12}\ \mathrm{C\,V^{-1}\,m^{-1}}$; ϵ_i is the relative permittivity of region i), $\boldsymbol{E}$ is the electric field and q_s is the interfacial charge density (Melcher & Taylor 1969). In perfect dielectrics no free charge carriers exist and the electric stresses act normal to the interface. In this study we will also consider poor conductors – also termed leaky dielectrics – that support accumulation of interfacial charges implying the presence of tangential electric stresses also (Saville 1997).

The electric force density $\boldsymbol{F}^{el}$ in (2.4) can be computed by applying the divergence operator to the Maxwell stress tensor T^M, i.e.

$$\boldsymbol{F}^{el} = \nabla \cdot T^M, \qquad T^M_{ij} = \epsilon\epsilon_0 \left(E_i E_i - \frac{1}{2}\left[1 - \frac{\rho}{\epsilon}\left(\frac{\partial \epsilon}{\partial \rho}\right)\right] E_i E_j \delta_{ij} \right). \tag{2.8}$$

The first term in the expression for T^M_{ij} represents the electric stresses due to free charge carriers and the second one models polarization stresses. The electrostriction stress given by the last term in (2.8) is neglected in this study since the fluids are incompressible. The electric force density is computed as follows. Since there is no external magnetic field, time-varying currents are negligible implying that the curl of the electric field is zero, i.e. $\nabla \times \boldsymbol{E} = 0$. Hence, the electric field can be computed from the scalar voltage potential V via $\boldsymbol{E} = -\nabla V$. Furthermore, we use the CSF approach that allows us, by smoothing the electric permittivity $\epsilon(\phi)$ and the conductivity $\sigma(\phi)$ across the interface, to apply the divergence form to the Maxwell stress tensor equation (2.8) on the entire flow domain. Thus, the computation of the electric force density requires solving a single Laplace equation for the electric potential $\nabla \cdot (\sigma \nabla V) = 0$.

We close this section by describing our non-dimensionalization. The governing equations are solved on a computational box with $L/2H = 1$, where L denotes the length and $2H$ is the width of the channel, respectively. The no-slip and no-penetration conditions are imposed at the rigid walls, and the flow is assumed periodic in the horizontal direction. A shear-driven flow with a linear velocity profile is generated in the channel by continuously moving the upper and lower channel plates with velocity U_{wall} and $-U_{wall}$, respectively, such that the net fluid flow in the channel is zero. An electric potential difference $\Delta V = -2HE_\infty$ is introduced into the channel gap by maintaining the upper wall at constant voltage potential, while the lower one is grounded. Lengths are scaled by the half channel width H, velocities by U_{wall} and the material properties of the suspending fluid 1 are taken as reference values. This leads to the following dimensionless groups describing the flow,

$$Re = \frac{\rho_1 U_{wall} H}{\mu_1}, \quad Ca = \frac{\mu_1 U_{wall}}{\Gamma}, \quad We_{el} = \frac{\epsilon_0 E_\infty^2 H}{\Gamma}, \quad R = \frac{\sigma_2}{\sigma_1}, \quad S^{-1} = \frac{\epsilon_2}{\epsilon_1}, \tag{2.9}$$

which represent the Reynolds number Re, the capillary number Ca which measures the ratio of viscous to surface tension forces, the electric Weber number We_{el} which characterizes the ratio of the electric to surface tension forces and the ratios of conductivities and permittivities.

3. Numerical method using the level set technique

We use the level set technique introduced by Osher & Sethian (1988) to both implicitly represent the fluid–fluid interface and to track its motion. First we embed the initial position of the interface as the zero level set of a continuous higher-dimensional scalar field $\phi(\boldsymbol{x}, t)$. Second, we associate the evolution of this function to the propagation of the interface itself through a time-dependent initial value problem, so that at any time the zero level set corresponds to the fluid–fluid interface Π, that is

$$\Pi = \{\mathbf{x} : \quad \phi(\boldsymbol{x}, t) = 0\}, \tag{3.1}$$

where $\phi > 0$, $\phi < 0$ represent the fluid regions 1 and 2, respectively.

The time evolution of the interface is modelled via transport of the level set function $\phi(\boldsymbol{x}, t)$ due to the underlying physical velocity field $\boldsymbol{u}(\boldsymbol{x}, t)$,

$$\frac{\partial \phi}{\partial t} + (\boldsymbol{u}_{\Pi} \cdot \nabla)\,\phi = 0, \quad \text{with} \quad \boldsymbol{u}_{\Pi} = \boldsymbol{u} \cdot \boldsymbol{n}. \tag{3.2}$$

Note that (3.2) takes into account only the normal component of the interfacial velocity to track the interface motion since the tangential velocity does not affect the shape of the interface.

The numerical method to solve the electrohydrodynamic problem is briefly described next. The spatial discretization of the governing equations is performed on a staggered Cartesian mesh. A cell-centred collocated arrangement is used for the pressure, the scalar potential, the material properties and the Maxwell stress tensor, while the velocities and the components of the electric field vector are located on the cell faces. The pressure gradient is discretized using values at the old time step such that the resulting velocity field is not divergence free, in general. For this reason, the velocity at the new time step is updated from the discretized continuity and momentum equations in such a way that the solution of the resulting pressure equation ensures a solenoidal velocity field that satisfies mass conservation; this leads to a Poisson problem that is solved by a standard multigrid technique (see Chorin 1968 for details of this projection method to solve the Navier–Stokes equations). In addition, we apply an essentially non-oscillatory (ENO) scheme of third-order accuracy (Osher & Shu 1991) for the treatment of the convective terms in the momentum equations. A standard level set equation is used to move the interface as described above, with time integration carried out using a second-order explicit Adams–Bashford method. The time step is adjusted to satisfy the CFL condition and constraints due to surface tension and the jump of the electric properties. Parallelization of the code is performed on conventional domain decomposition using MPI.

At each iteration step, the velocity and pressure fields are first computed by marching the discretized Navier–Stokes equations by one time increment. Then, the level set equation (3.2) is advanced using the newly computed fluid velocity field. The difficulty with this procedure is that ϕ does not remain a signed distance function as it is marched in time and hence errors accumulate. These errors are usually observed as loss or gain of mass. Different strategies of correcting the numerical method have been developed in order to conserve mass. A widely used approach is to reinitialize the level set function after each time step (Sussman *et al.* 1994). Ideally, the interface should not change its position during this reinitialization procedure, but in many applications the zero level set can become distorted by parasitic numerical inaccuracies if the gradients in the neighbourhood of the interface are either very large or very small. For this reason, an improved reinitialization method was proposed by Sussman & Fatemi (1999), where the mass conservation is enforced by artificially modifying the interfacial velocity. Although this method inherently preserves mass, it introduces a non-physical correction term to the interfacial velocity. A different approach was developed by Sethian (1996, 1999), who built velocities for the neighbouring level set when the physical velocity is defined solely on the interface itself by using the fast marching method (see below). These extension velocities replace the fluid velocity in the level set equation by the normal velocity of the interface. The advantage of this approach is that the level set function is marched in time according to a given velocity field that is prescribed on the interface. Hence, the signed distance property of the level set function is maintained, and the need for reinitialization is drastically reduced or eliminated. Noticing that the values of the level set function are only needed

in the neighbourhood of the interface, the narrow-band method was introduced by Adalsteinsson & Sethian (1995). In this approach the level set function is advanced only in a narrow band of a few mesh points of the interface. Both the narrow-band and velocity extension methods are used in the present computations.

Next we briefly describe the implementation of the narrow-band level set method and refer the reader to the literature for more details. The level set function is constructed by starting from the initial position of the interface and computing the signed distance function, employing the very efficient fast marching technique (Sethian 1996). To advance the level set function velocities are required throughout the narrow band. Since the velocities are initially defined only on the interface itself, we use the extension technique introduced by Adalsteinsson & Sethian (1999) to define the velocity for all the level sets, not just the one representing the interface. Along the interface the normal velocity is defined as

$$F = \boldsymbol{u} \cdot \nabla \boldsymbol{\phi} / |\nabla \phi| \,. \tag{3.3}$$

The interfacial velocity F is computed by evaluating (3.3) using the bicubic interpolation method of Chopp (2001). The basic idea is to use information at the mesh points in the neighbourhood of the interface to construct a bicubic interpolation polynomial, and then, to exploit this polynomial for each mesh point adjacent to the interface to find the closest point on the interface and its velocity F. After we initialize adjacent grid points by projecting the interfacial velocity values just found, we use the fast marching method to update the values of ϕ^{temp} and F_{ext} in the entire narrow-band set. That is, the extension velocities are built by simultaneously constructing a temporary signed distance function, ϕ^{temp} say, and an extension velocity as solution of the Eikonal equation $\nabla \phi^{temp} \cdot \nabla F_{ext} = 0$. Using the extension velocity F_{ext} the level set equation (3.2) can be rewritten as

$$\frac{\partial \phi}{\partial t} + F_{ext} |\nabla \phi| = 0. \tag{3.4}$$

Finally, the level set band is marched in time by solving (3.4) with a second-order Adams–Bashford multistep scheme.

4. Numerical results

We begin by studying the dynamics of a periodic array of drops in a Couette device without an electric field in order to identify the driving mechanisms that cause the deformation of an initially circular drop and to validate the code. Subsequently we impose a vertical electric field and simulate its effects on the drop deformation, for both perfect and leaky dielectric fluids. There is a large set of parameters to consider and in the results that follow we assume that the drop phase and the suspending fluid have the same viscosity and density. The radius a of the initially circular drop is taken to be equal to a quarter of the channel height, i.e. $a/H = 1/2$, which leads to an area ratio $A_{drop}/A_{channel} = \pi/16$. We note that several authors have extensively studied the same set-up in the literature – detailed results are documented in Zhou & Pozrikidis (1993*a*, 1994), Kennedy *et al.* (1994) and Sheth & Pozrikidis (1995).

The simulations are initialized by suddenly introducing the drop into the Couette device. Stressed by the incident shear, the drop immediately begins to elongate in the direction of the major principal axis of the rate of strain of the mean flow. That is, the drop deforms into an ellipsoidal shape while generating a non-uniform curvature of the interface to compensate the interfacial shear stresses. To check the sensitivity

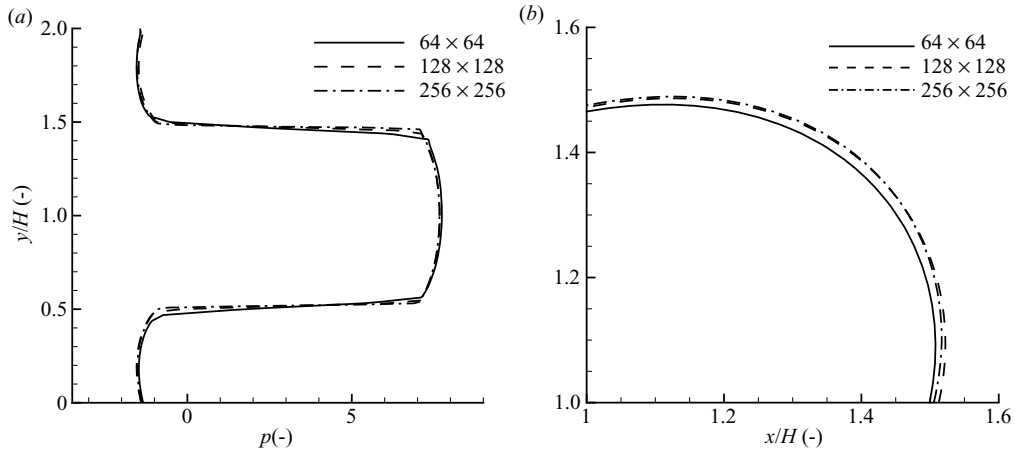

FIGURE 2. Cross-sectional pressure profile at $x/H = 1$ (a) and a section of the drop shape (b) at non-dimensional time $t = 1.5$. The solutions were computed on three different meshes with 64×64, 128×128 and 256×256 nodes, respectively. $Re = 1$, $Ca = 0.2$, $We_{el} = 0$.

of the numerical solutions on the mesh size, the vertical variation of the computed steady-state pressures at the horizontal position $x/H = 1$ (i.e. the centre of the channel) is compared in figure 2(a) for three different meshes having 64×64, 128×128 and 256×256 nodes each. Other parameter values are $Re = 1$, $Ca = 0.2$ and $We_{el} = 0$. It is seen that the pressure has jumps at the vertical positions $y/H \approx 0.5, 1.5$ where the interface is located – the jumps are smeared out for the coarse mesh (64×64) but are sharply resolved for the medium (128×128) and fine (256×256) meshes. A section of the drop shape is shown in figure 2(b) for the three different discretizations. The drop shapes on the medium and fine meshes are almost identical, but differences are evident when compared to the coarse grid solution. The percent area gain/loss ($+/-$) of the drop area from its initial size was found to be $+0.19$ on the coarse mesh, $+0.15$ on the medium mesh and $+0.04$ on the fine mesh, respectively. Since time-dependent highly accurate solutions are computationally expensive we employ the 128×128 mesh for all the computations reported in what follows, unless stated otherwise.

When an initially circular liquid drop is suddenly introduced into a simple shear flow it deforms with a time-dependent shape and orientation. A deformation takes place whether an electric field is absent or not and in the ensuing discussion we consider the $We_{el} = 0$ case. Whether an equilibrium state exists or the drop elongates indefinitely, depends on the values of dimensionless parameters such as the Reynolds and capillary numbers Re and Ca, and the viscosity ratio λ, for example. At small values of Ca the deformation approaches an ellipsoidal equilibrium shape, while at sufficiently large values of Ca the drop continues to elongate indefinitely and most probably breaks up when additional effects such as Van der Waals attraction forces become important. Inertial effects are negligible at small Reynolds numbers and the interplay of surface tension forces and viscous forces determines the drop dynamics. In this regime the drop elongates along the principal extension direction and is squashed in the direction normal to it. In addition, a single vortical swirl flow is formed inside the drop. When Re is increased, the drop rotates towards the mean-flow direction and the velocity field inside the drop generates additional swirls. Highly elongated equilibrium shapes appear at smaller angles θ between the major axis of the drop and the horizontal. Inertial effects are dominant at the poles where the drop experiences

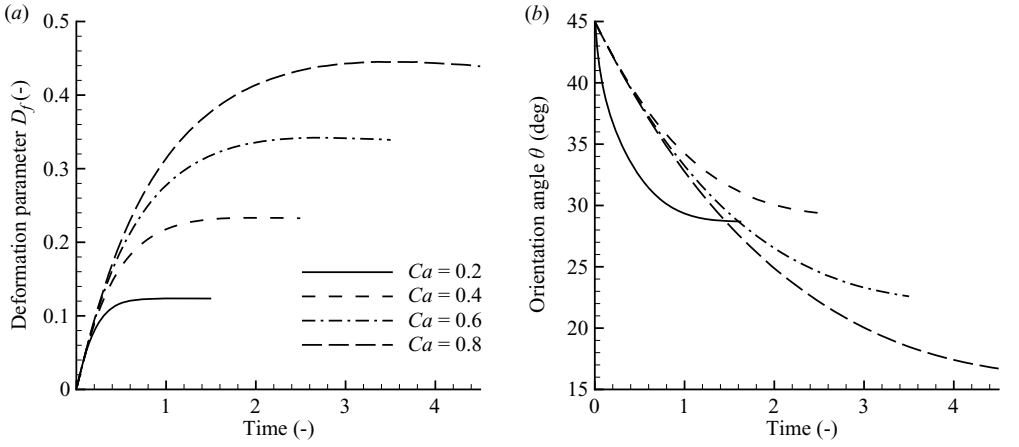

FIGURE 3. Evolution of the deformation parameter D_f (a) and the orientation angle (b) θ of a periodic array of liquid drops suspended in simple shear flow at $Ca = 0.2$, 0.4, 0.6, 0.8, $Re = 1$, $We_{el} = 0$.

the highest flow rates and this explains the sigmoidal equilibrium shapes that are observed in this regime. It has been established by our calculations (in complete agreement with other authors) that for $Ca > 0.2$ and $\lambda = 1$, significant deviations from the theoretically predicted elliptical shape appear. Moreover, for $Ca > 0.5$, the viscous forces responsible for the drop deformation exceed the shape preserving surface tension forces and the drop elongates significantly. In our computations in this regime we observe indefinite elongation – the level set technique is capable of going through a topological transition but this is a very delicate phenomenon to reconcile with the underlying physics. We typically halt our computations when the drop elongates indefinitely and conclude that no steady state exists in such cases.

Following Taylor (1966) the parameter $D_f = (L_{max} - L_{min})/(L_{max} + L_{min})$, where L_{max} is the length of the major axis and L_{min} the length of the minor axis of an approximated ellipsoid, provides an appropriate measure of a slightly deformed drop. The orientation of the drop, which characterizes the effectiveness of a particular flow (or electric field strength in the absence of a background flow as in Taylor 1966) in deforming it, is given by the angle θ between the ellipsoid major axis and the horizontal axis. According to Rhodes, Snyder & Roberts (1989) who study the deformation of droplets by an electric field in a quiescent medium, the deformation is elliptical for small interfacial distortions, while for large deformations the shape deviates substantially from an elliptical one. To quantify the evolution of the drop deformation we construct the parameter D_f introduced by Taylor even in situations where the drop is not strictly elliptical, by estimating L_{max} and L_{min} for an equivalent least-squares fitted elliptical shape. True elliptical shapes are recovered for slightly deformed drops at small capillary numbers but deviations from ellipses occur when strong shearing or electric stresses act on the drop interface as our results show below.

The evolution of the deformation parameter D_f and the orientation angle θ between the major axis and the horizontal axis is plotted in figure 3 for the flow characterized by the capillary numbers $Ca = 0.2$, 0.4, 0.6, 0.8 and $Re = 1$. The simulations indicate that the drop evolves smoothly from a circular to an elliptical shape. For $Ca = 0.2$ the drop reaches an equilibrium state after approximately 1.0 time unit from its introduction into the Couette device. As the capillary number increases, higher

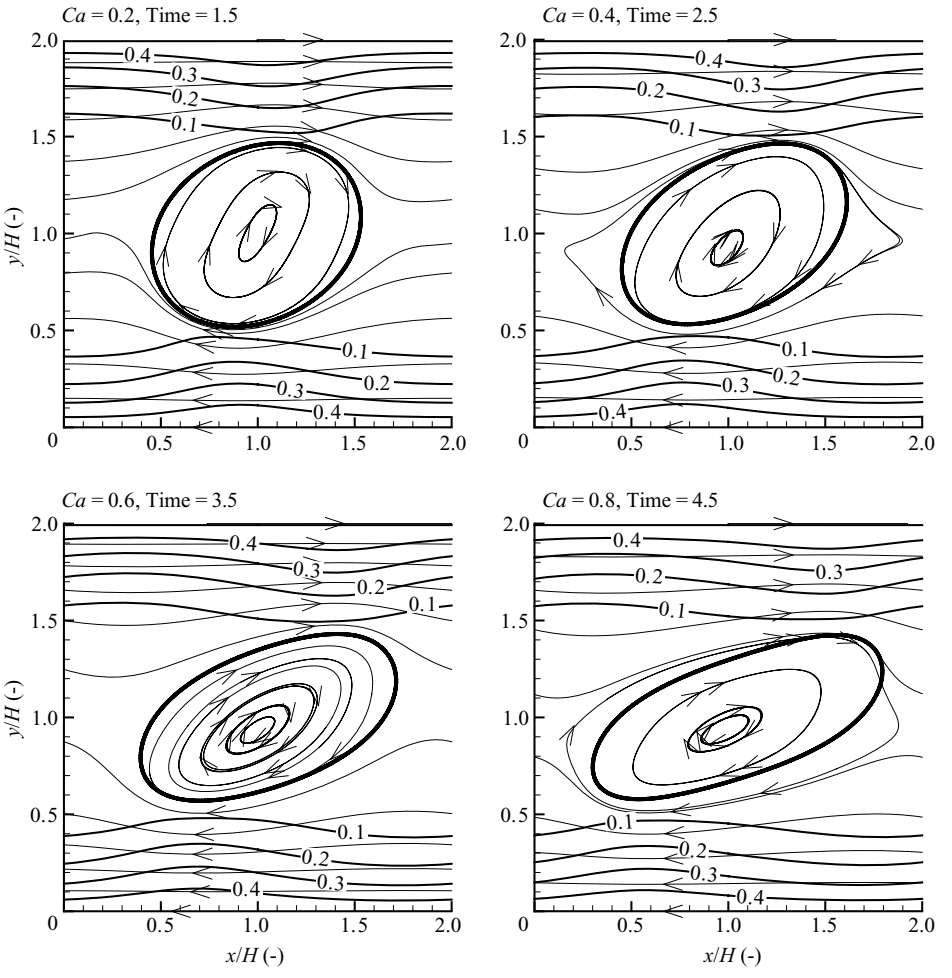

FIGURE 4. Streamline patterns and contours of the kinetic energy of a periodic array of liquid drops suspended in simple shear flow at $Ca = 0.2, 0.4, 0.6, 0.8$, $Re = 1$, $We_{el} = 0$.

interfacial curvatures are locally necessary to balance the shear stress and the time to equilibrium increases. Furthermore, the direction in which the drop elongates is governed by the incident shear, explaining why the orientation angle begins at $\theta = 45^\circ$ (defined thus so that it coincides with the direction of the shear) and decreases as the capillary number increases causing larger deformations. According to these results, the orientation angle appears to have a non-monotonic behaviour as Ca increases. The streamline plots of figure 4 below, however, indicate that the orientation angle decreases monotonically with Ca. This discrepancy is due to the limitation of the definition of the orientation angle which is calculated by first fitting the drop shape to an ellipse, as is conventional in the literature. We note that analogous results were obtained by Sheth & Pozrikidis (1995).

In figure 4 we show streamline patterns and contours of the kinetic energy $E_{kin} = (1/2)\boldsymbol{v} \cdot \boldsymbol{v}$, corresponding to the run shown in figure 3. Since the incident velocity varies linearly in the vertical direction from $-U_{wall}$ to $+U_{wall}$ (or -1 to $+1$ in dimensionless terms), regions of high energy are confined to the horizontal walls. Due to the action of the interfacial forces a single clockwise rotating eddy

is formed inside the drop. For $Ca = 0.2$ at $t = 1.5$, the interface is tangential to the local streamlines and separates the recirculation zone from the translating fluid region. Moreover, the streamline patterns at time $t = 1.5$ do not cross the interface indicating that the deformed drop has reached its equilibrium shape in agreement with the results in figure 3. The streamline patterns for $Ca = 0.4$ at $t = 2.5$ also indicate that an equilibrium shape has been attained, again in agreement with the results of figure 3. For $Ca = 0.6$ at $t = 3.5$ there is a slight streamline crossing, while for $Ca = 0.8$ at $t = 4.5$ streamline crossing is very evident. In fact for $Ca = 0.8$ the drop elongates indefinitely; the case $Ca = 0.6$ is very close to the threshold value above which such infinite elongation occurs, and a significantly longer computation is required to determine if a steady state is reached.

4.1. *Perfect dielectric fluids*

To study the effects of an electric field on drop deformation we repeat the numerical simulations discussed above but now impose a constant voltage potential difference between the channel walls. In the absence of a drop an electric field with lines of constant potential parallel to the wall electrodes is generated. We introduce a liquid drop and assume that the two fluids are perfect dielectrics characterized by the permittivity ratio $S^{-1} = \epsilon_2/\epsilon_1 = 2$. The electric Weber number We_{el} is set to 50, while the Reynolds number Re is 1. In addition to surface tension and viscous stresses, the electric field in perfect dielectric liquid–liquid systems acts to generate stresses that act perpendicular to the interface. It can be shown theoretically that in such cases, and in the absence of a background shear, a liquid drop always evolves into a prolate shape irrespective of the permittivity ratio (Taylor 1966). We also note that the electric stresses have maximum values around the poles of the drop, and since surface tension counteracts stretching, the largest shape curvature occurs in this region. If the intensity of the electric field is large the extremities of the drop are found in the outer flow regions, that is in regions of higher flow rates. Hence, inertia gains importance locally and the drop looses its elliptical shape and attains a sigmoidal shape (this can be seen in the bottom right panel of figure 5, for example).

The initially uniform electric field is disturbed due to the presence of the drop which introduces a disparity in the dielectric permittivity between the two phases. In figure 5 we show the direction of the disturbed electric field (lines with arrows) and its intensity $|\boldsymbol{E}|$ (contours) for a flow characterized by $Ca = 0.2, 0.4, 0.6$ and 0.8 at $t = 1.5, 2.5, 3.5$ and 4.5, respectively. In all four cases the electric Weber number is 50 and $Re = 1$. Inside the drop the electric field lines are straight, but the direction of the electric field changes across the interface in order to satisfy Gauss's law that reduces to the continuity of the displacement field in this case (see § 2). In addition, the electric field attains its maximum intensity around the drop interface in regions that are closest to the electrodes, where it induces the largest interfacial stresses. The increase of the drop deformation and the decrease in the orientation angle θ between the major axis of the drop and the horizontal from $Ca = 0.2$ to $Ca = 0.8$ is clearly visible. We remark that without flow the drop attains a symmetric prolate shape. The incident shear flow accounts for the break of this symmetry and the ensuing hydrodynamic coupling.

The corresponding streamline patterns and contours of the kinetic energy for the previous computation ($Ca = 0.2, 0.4, 0.6, 0.8$, $We_{el} = 50$, $Re = 1$) are presented in figure 6. It can be seen from the streamline patterns that steady states have been reached for the two smallest capillary numbers, whereas for $Ca = 0.6$ at $t = 3.5$ some streamline crossing is still discernible while for $Ca = 0.8$ the drop is still deforming at

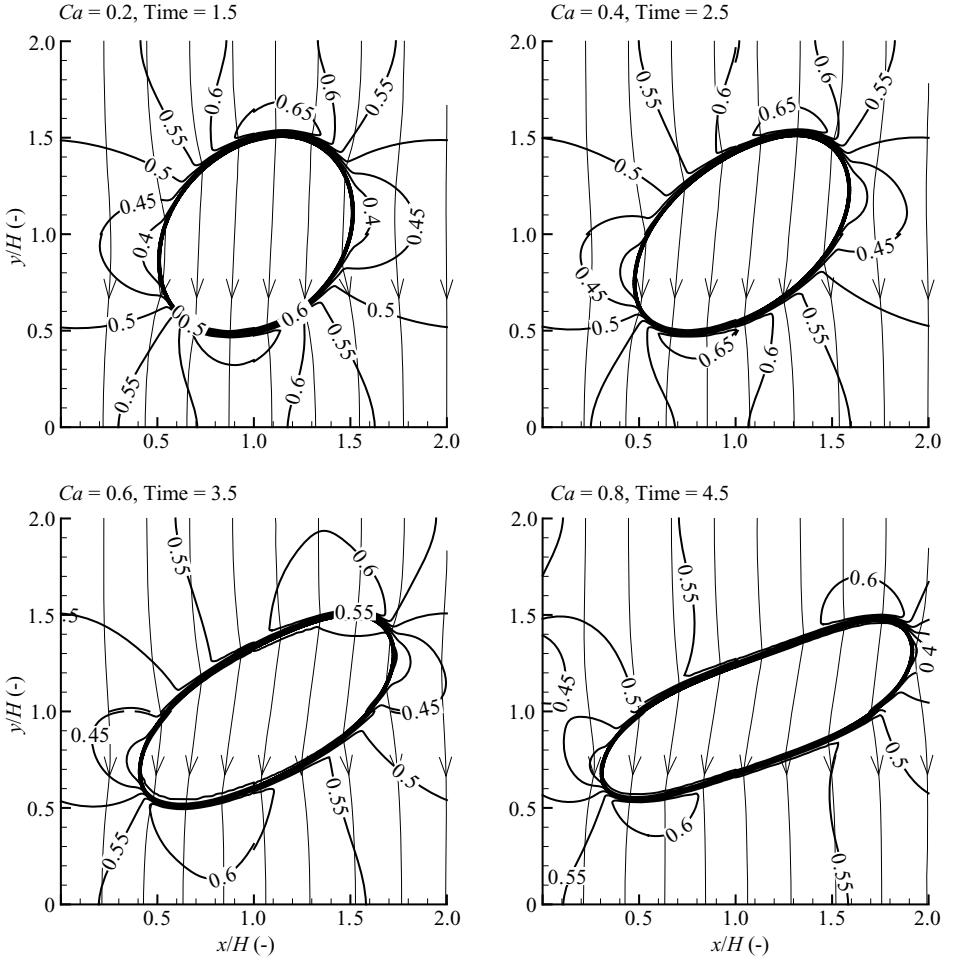

FIGURE 5. Direction (lines with arrows) and intensity (contours) of the disturbed electric field confined between the two horizontal wall electrodes of a Couette device at $Ca = 0.2, 0.4, 0.6, 0.8$ with $Re = 1$. Electric Weber number $We_{el} = 50$.

a time $t = 4.5$. The presence and deformation of the drop due to the shear and the electric field, tends to block the incident shear so that regions of high kinetic energy are established in the gap between the drop and the wall, in turn affecting the shear stress on the wall.

Next we consider the effect of the electric Weber number We_{el} on the evolution of the drop and in particular the deformation parameter D_f. The results are presented in figure 7 and have capillary numbers $Ca = 0.2, 0.4, 0.6, 0.8$, electric Weber numbers $We_{el} = 0, 10, 25, 50$, Reynolds number $Re = 1$ and a permittivity ratio $S^{-1} = 2$ as before. With the exception of the smallest capillary number case $Ca = 0.2$, the deformation is found to monotonically increase with increasing We_{el} ultimately yielding more deformed equilibrium shapes (if they exist). We also note that the time to equilibrium increases with We_{el}. For $Ca = 0.2$, and for the electric Weber numbers $We_{el} = 10, 25$ the deformation is slightly smaller than for $We_{el} = 0$. One explanation for this is that there is a competition between the shear that tends to deform the drop in its direction, and the field which according to the results of Taylor

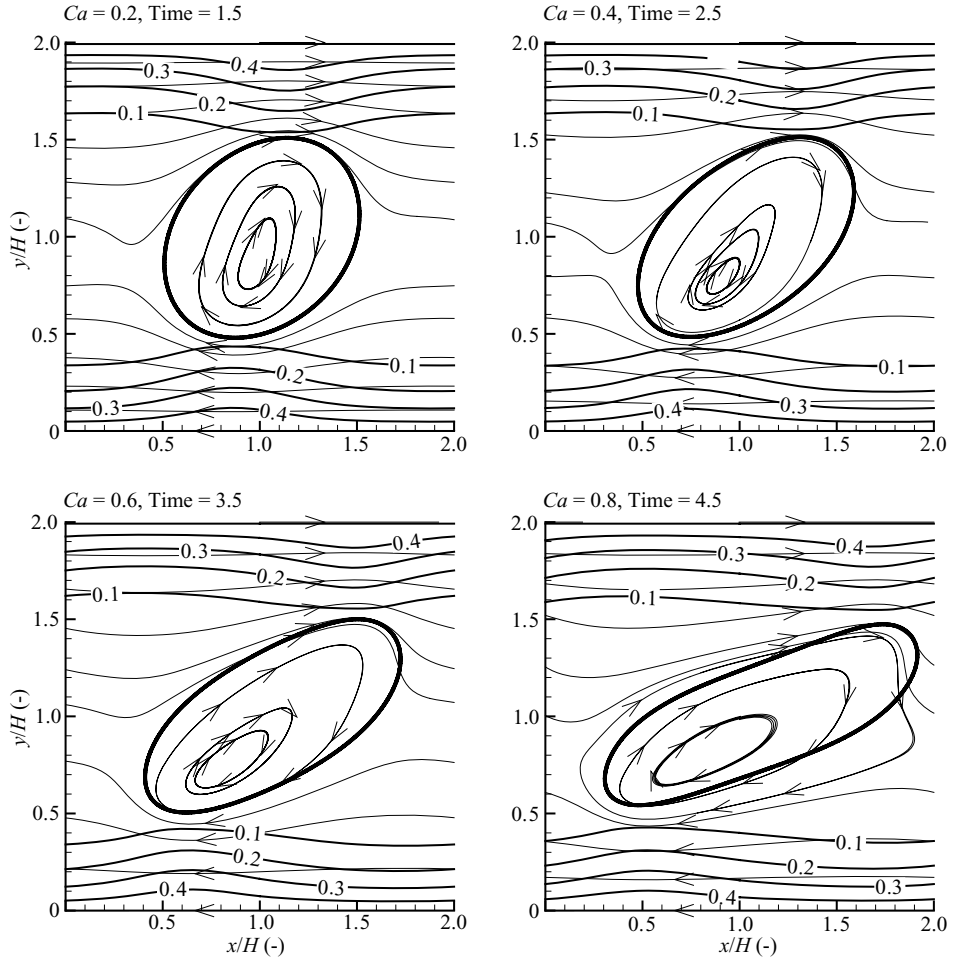

FIGURE 6. Streamline patterns and contours of the kinetic energy of a periodic array of liquid drops in simple shear flow at $Ca = 0.2, 0.4, 0.6, 0.8$, $Re = 1$ when an electric field at $We_{el} = 50$ is present in the gap.

(1966) tends to induce prolate deformations, so that at small values of Ca and We_{el} the cumulative effect is a slightly smaller deformation. On the other hand the results for the highest value of $Ca = 0.8$ indicate that the deformation reaches a maximum value at a certain time and then starts decreasing. We emphasize, however, that this is due to the definition of D_f and its construction for non-elliptical shapes. The drop shapes shown in figure 6 at $Ca = 0.6, 0.8$, for instance, are sigmoidal and so the applied least-squares fit based on elliptical shapes leads to the variations in the deformation parameter outlined above.

The orientation angles that correspond to the results of figure 7 are shown in figure 8. The initially circular drop is introduced into the flow at $t = 0$, and so all the curves pass through the $\theta = 45^\circ$ point at $t = 0$ (after the first time step the flow induces stretching in the shear direction and so the orientation angle at $t = 0^+$ is $\pi/4$). The qualitative characteristics are similar for all four values of Ca. The angle increases monotonically as We_{el} is increased so that for a given Ca, the curves are ordered with the smallest angles attained at $We_{el} = 0$ and the largest at $We_{el} = 50$. This is due

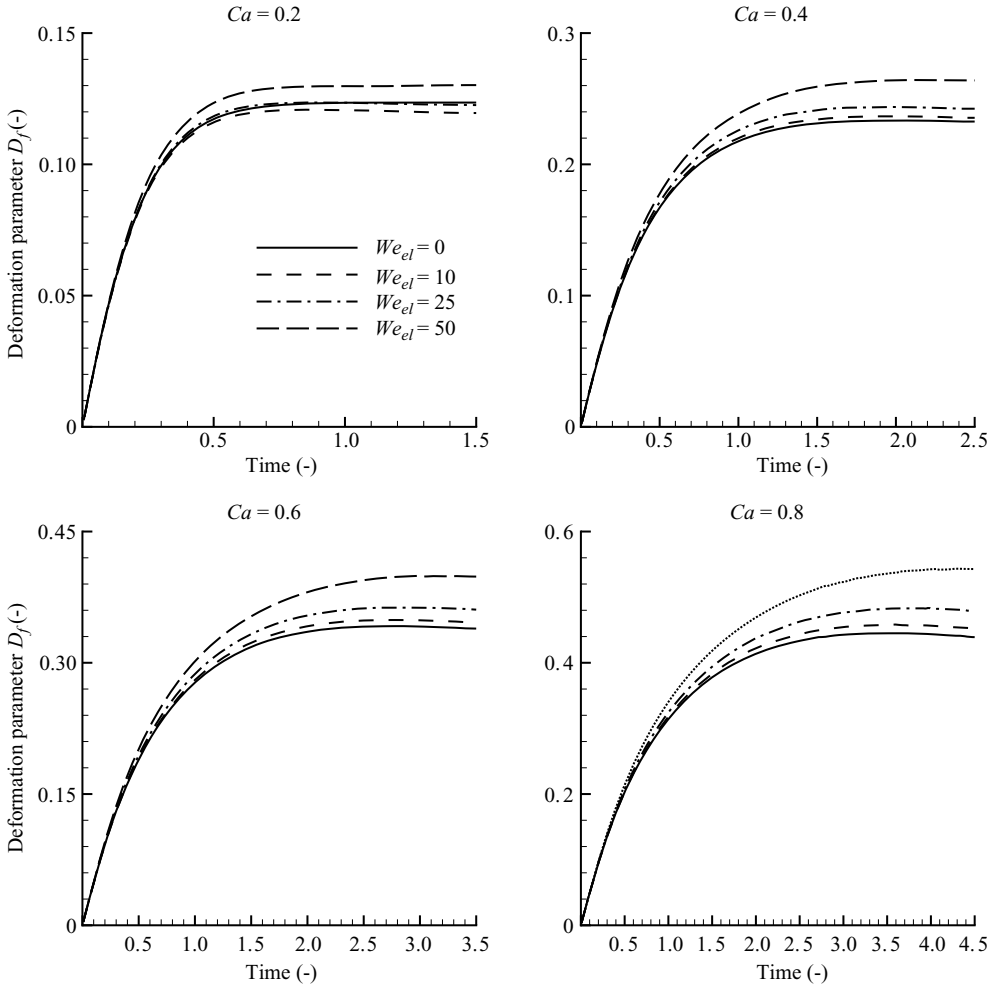

FIGURE 7. Evolution of the deformation parameter D_f of a periodic array of liquid drops suspended in simple shear flow at $Ca = 0.2, 0.4, 0.6, 0.8$, $Re = 1$ when an electric field given by $We_{el} = 0, 10, 25, 50$ is present in the gap.

to the stretching of the drop towards the wall electrodes caused by an increasing electric field. In addition, the presence of an electric field causes an overshoot in the orientation angle after the drop is initially introduced into the flow, whereas the non-electrified case gives monotonically decreasing orientation angles throughout the evolution.

Next we consider the flow structure by studying the vorticity field inside and outside the drop. Vorticity is generated due to the deformation, the interfacial stresses and by the interaction of the disturbed Couette flow with the rigid channel walls. The distribution and strength of vorticity inside and outside the drop are relevant to problems such as mixing or heat and mass transfer (Ward & Homsy 2001, 2003). Figure 9 shows the vorticity distribution in the flow for the capillary numbers $Ca = 0.2, 0.4, 0.6, 0.8$ at an electric Weber number $We_{el} = 50$. (The Reynolds number is set to unity as before.) Two regions of high-vorticity production can be identified in the flow. Large positive values occur in the vicinity of the poles of the deformed drop

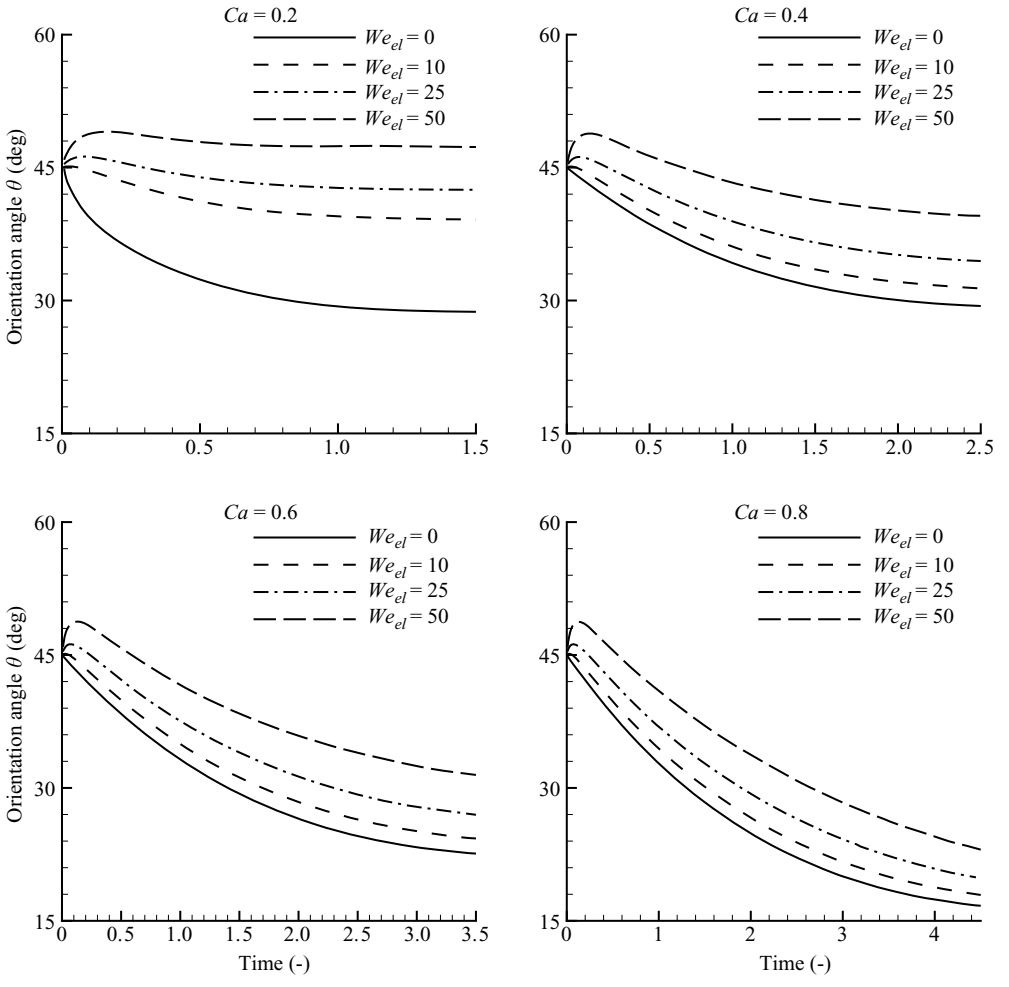

FIGURE 8. Evolution of the orientation angle θ of a periodic array of liquid drops suspended in simple shear flow at $Ca = 0.2, 0.4, 0.6, 0.8$, $Re = 1$ when an electric field given by $We_{el} = 0, 10, 25, 50$ is present in the gap.

and these positive vorticity maxima are paired with spots of negative vorticity directly above (or below) them in the vicinity of the wall. Large negative vorticity regions are also found at the equator of the deformed drop. Furthermore, the transport as well as the diffusion of vorticity in the centre region of the channel is clearly evident in figure 9, and in particular at the larger capillary numbers $Ca = 0.6, 0.8$. Similar vorticity generation regions in deformed drops have been identified by Ryskin & Leal (1984) in a non-electrified problem.

In the results presented in figure 10 we consider the effect of variations of the permittivity ratio S^{-1} on drop deformation. All the results in the figure fix $Re = 1$ and $Ca = 0.2$. Physical examples of such systems are castor oil drops in silicone oil 1 M ($S^{-1} = 2$) or a silicone oil 1 M drop in castor oil ($S^{-1} = 0.5$) (see Burcham & Saville 2000 and the discussion of physical systems in § 4.2 below. The range $S^{-1} = 0.1, 0.5, 2, 10$ is covered at $Re = 1$, $Ca = 0.2$, $We_{el} = 10$, $\lambda = 1$, and it is seen from the results that the deformation parameter D_f at steady state, if this exists, is not a

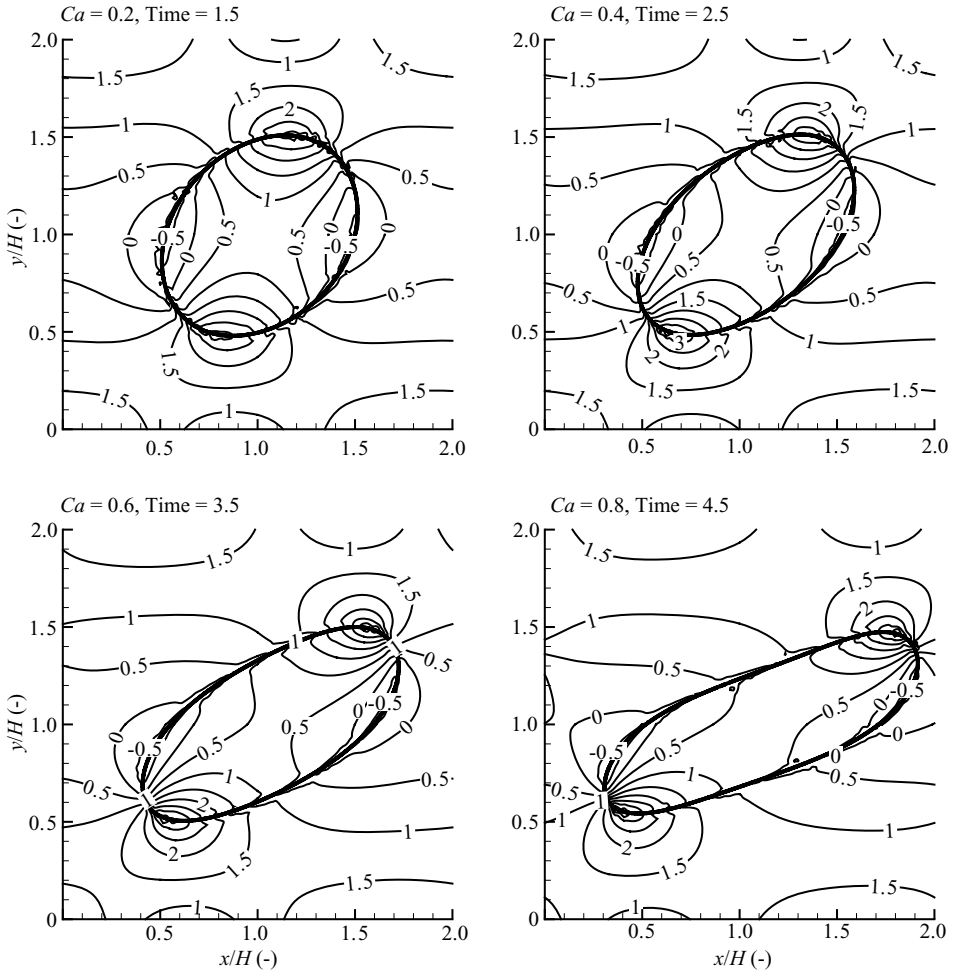

FIGURE 9. Vorticity distribution in the liquid drop suspension at $Ca = 0.2, 0.4, 0.6, 0.8$, $Re = 1$ when an electric field given by $We_{el} = 50$ is present in the gap.

monotonic function of S^{-1}. Starting with the smallest values of $S^{-1} = 0.1$ we observe that the steady-state values of D_f decrease slightly as S^{-1} is increased to 0.5 and 2, respectively. As S^{-1} is increased further to a value of 10 we see that the deformation parameter approximately doubles on its way to attaining its steady-state value which is yet to occur when the computation is halted at $t = 1.5$. This non-monotonic behaviour is also emphasized in the results of the orientation angle shown in figure 10(b). The orientation angle at the smallest value of $S^{-1} = 0.1$ is about 50°, and it decreases significantly to values of approximately 40° and 30° as S^{-1} increases to values of 0.5 and 2. The non-monotonicity is evident in the evolution of the orientation angle for $S^{-1} = 10$ which reaches an angle of more than 60° by the end of the computation. We conclude, therefore, that for a fixed set of physical parameters and values of the relative permittivity satisfying $S^{-1} > 1$, the drop deformation and its angle of orientation can be increased by increasing the permittivity of the drop liquid relative to the suspending fluid. In such instances, this implies more slender drops that tend to align with the underlying electric field. Our computations also indicate that for sufficiently large values of S^{-1} the deformed drop elongates indefinitely without a

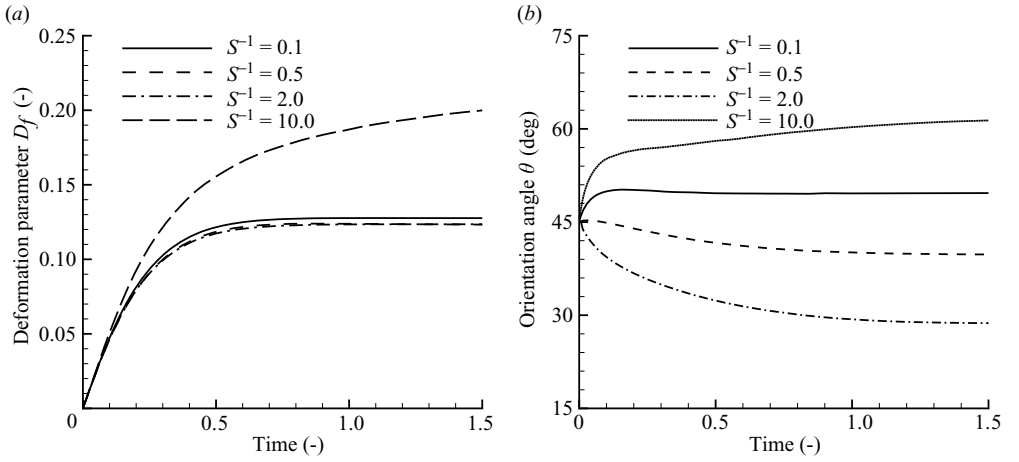

FIGURE 10. Effect of the permittivity ratio $S^{-1} = \epsilon_2/\epsilon_1$ on the evolution of the deformation parameter D_f (a) and the orientation angle θ (b) of a periodic array of liquid drops suspended in simple shear flow. Values of S^{-1} indicated on the figure; $Re = 1$, $Ca = 0.2$, $We_{el} = 10$.

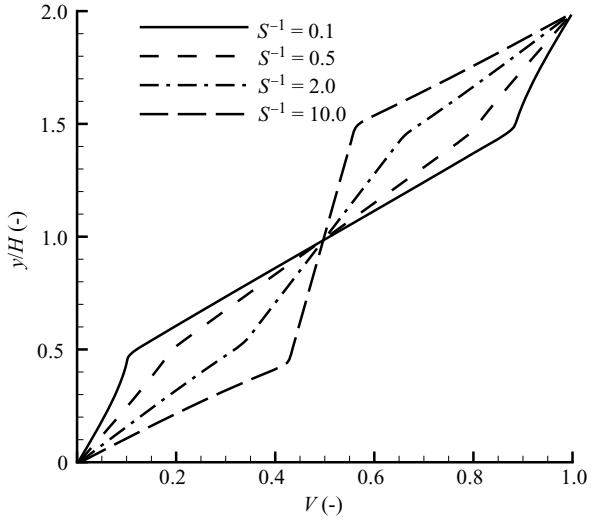

FIGURE 11. Effect of the permittivity ratio $S^{-1} = \epsilon_2/\epsilon_1$ on the vertical distribution of the electric potential V between the horizontal electrodes at $x/H = 1$. Values of S^{-1} indicated on the figure; $Re = 1$, $Ca = 0.2$, $We_{el} = 10$.

steady state being reached. One possible explanation for this behaviour is the increased effect of the electrical stresses at the interface and their role in deforming the drop. A comparison for different values of S^{-1} is provided in figure 11. The figure shows the variation of the electric potential with the vertical coordinate in the middle of the channel, that is $V(x = H, y)$, corresponding to the runs of figure 10. The values of S^{-1} are indicated on the figure and several features are worth pointing out. First, in all cases the position of the drop interface is located where there is a sharp change in the slope of the potential (i.e. a sharp change in the electric field). The numerical method smoothes this out as is evidenced in the figure. In addition, the magnitude of the field inside the drop increases as S^{-1} is increased, while the field intensity outside

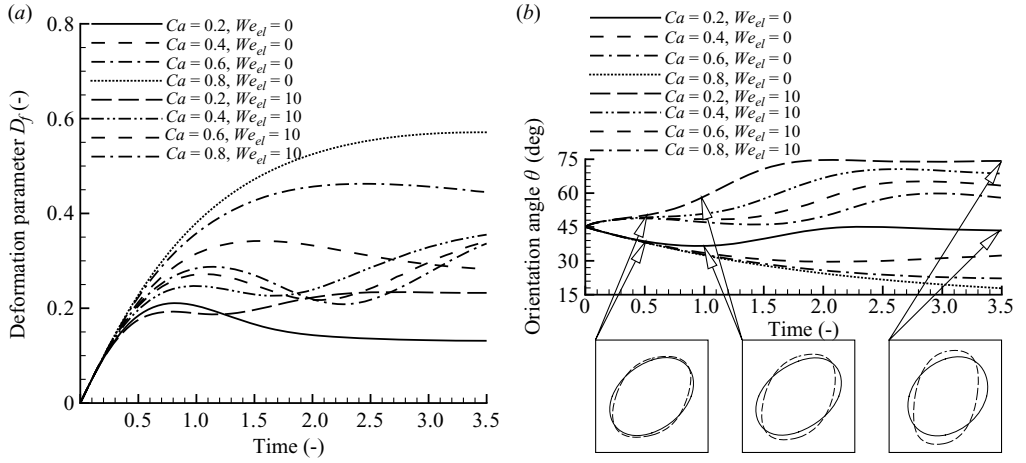

FIGURE 12. Effect of the capillary number Ca and electric Weber number We_{el} on the evolution of the deformation parameter D_f (a) and the orientation angle θ (b) of a periodic array of liquid drops suspended in simple shear flow at $Re = 10$. Values of Ca and We_{el} indicated on the figure; $S^{-1} = 2$, $\lambda = 1$. The inserts on (b) show the drop profiles for $We_{el} = 0$ (solid) and $We_{el} = 10$ (dashed) at times $t = 0.5, 1, 3.5$.

the drop decreases. The jump in the field drives the Maxwell stresses at the interface which in turn affect drop deformation – the results of figure 11 suggest that among the different values of S^{-1} considered this effect is largest for the case $S^{-1} = 10$.

We conclude this section by presenting a set of computations at a Reynolds number $Re = 10$ in order to evaluate the effects of increased inertia. The computational resolution is the same as for the $Re = 1$ cases (a grid of 128×128 is used). For definiteness we consider the permittivity ratio $S^{-1} = 2$ and compute the evolution of the deformation parameter D_f and the orientation angle θ for different values of the capillary and electric Weber numbers. The results are shown in figure 12. Specifically, we consider the flow for the capillary numbers $Ca = 0.2, 0.4, 0.6, 0.8$, and for each of these compute two sets of results: electric field absent $We_{el} = 0$ and present with $We_{el} = 10$. We observe (in line with the computations of Lee & Pozrikidis 2006) that in the absence of an electric field there is an overshoot in the evolution of the deformation and orientation angle when inertia is present. At the lower values of $Ca = 0.2, 0.4$ the electric field increases the deformation at steady state, whereas at the larger values $Ca = 0.6, 0.8$ the deformation in the absence of a field is larger than that in its presence throughout the evolution (due to computational costs we have not integrated beyond $t = 3.5$ and hence cannot preclude the possibility of a crossover and a larger deformation in the presence of a field for $Ca = 0.6$ and 0.8 at a much larger time). The analogous results for the orientation angle θ of the drop with the horizontal are collected in figure 12(b). Two conclusions can be drawn from the figure: First, irrespective of the value of Ca, the presence of the electric field increases the orientation angle and hence tends to align the major axis of the drop with the direction of the imposed electric field. Second, the behaviour is monotonic, that is the smallest Ca results have the largest orientation angles, irrespective of whether the field is present or not. This can be seen in the figure since the curves corresponding to $We_{el} = 10$ are all higher (at steady state) than those for $We_{el} = 0$. Furthermore, the orientation angle decreases as Ca increases, in all cases. Representative solutions of the drop shape at three times during the evolution are included as inserts in the

figure for the case $Ca = 0.2$. Drop shapes are shown at $t = 0.5, 1$ and 3.5 with the solid and dashed curves denoting $We_{el} = 0$ and 10, respectively. It is clear that the drop deforms as the evolution progresses and by $t = 3.5$ when a steady state has been reached the difference in the orientation is pronounced – the electrified system has a more elongated and more vertically aligned drop.

4.2. *Leaky dielectric fluids*

In this section we present computations based on the leaky dielectric model. As mentioned in § 1, Taylor analysed the static configuration of spherical drops in the zero Reynolds number limit and derived analytically a relation that discriminates between prolate and oblate forms. A similar analytical relation for two-dimensional drops was later given by Rhodes *et al.* (1989),

$$\Phi = R^2 + R + 1 - 3S^{-1}, \tag{4.1}$$

where the suspending fluid and the drop phase are assumed to have the same viscosity ($\lambda = 1$) – recall that S denotes the permittivity ratio ϵ_1/ϵ_2 and R denotes the conductivity ratio σ_2/σ_1. Equation (4.1) predicts prolate drops for $\Phi > 0$, and oblate ones for $\Phi < 0$, while $\Phi = 0$ represents zero deformation. The leaky dielectric model supports a jump in tangential electric stresses and hence we anticipate differences in drop deformation behaviour between leaky and perfect dielectric systems. The computations that are described next provide a quantitative comparison for several typical cases.

Here, two (R, S^{-1})-pairs of leaky dielectrics with (0.5, 2) and (2, 0.5) are considered, defined as systems A and B, respectively. Systems A and B are chosen as representative examples rather than values provided by particular fluid samples. System A represents a drop whose conductivity is smaller but its permittivity is larger than the surrounding fluid, while system B represents a drop whose conductivity is larger but its permittivity is smaller than the suspending fluid. Examples of such systems are a castor oil drop in silicone oil 1 M (system A) or a silicone oil 1 M drop in castor oil (system B). Specifically, using experimental values for these oils measured by Burcham & Saville (2000) gives approximate values of $R = 35$ and $S^{-1} = 2$ for the analogue to system A, and $R = 0.03$, $S^{-1} = 0.5$ for that of system B. We note also that for these oils the density and viscosity ratios are roughly equal. On the other hand, a silicone oil 12 M gives approximate values of $R = 18$ and $R = 0.06$ for systems A and B, respectively, but the viscosity of silicone oil 12 M is now about 12 times larger than that of the castor oil. We note that the conductivity of the silicone oils can be enhanced using doping in order to obtain a large range of values of R that includes the computational parameters picked here (see Shankar & Sharma 2004).

Figure 13 compares the streamlines (thin lines with arrows) and the contours of the kinetic energy (thick solid lines) in the flow for system A (left panel) and system B (right panel) computed for the electric Weber numbers $We_{el} = 25$ and 50. The results indicate that the effect of the electric field on the drop is different for the two systems. For system A the drop is stretched towards the electrodes leading to a prolate shape, but a deformation in the horizontal direction dominates for system B so that the drops achieve an oblate shape. The relatively enhanced channel blockage for system A causes regions of high velocity in the vertical gap between the drop and the channel walls and an intricate streamline pattern in the wake of the drop. In contrast, for system B the streamlines close to the wall are less affected by the drop's presence due to its alignment with the mean flow direction.

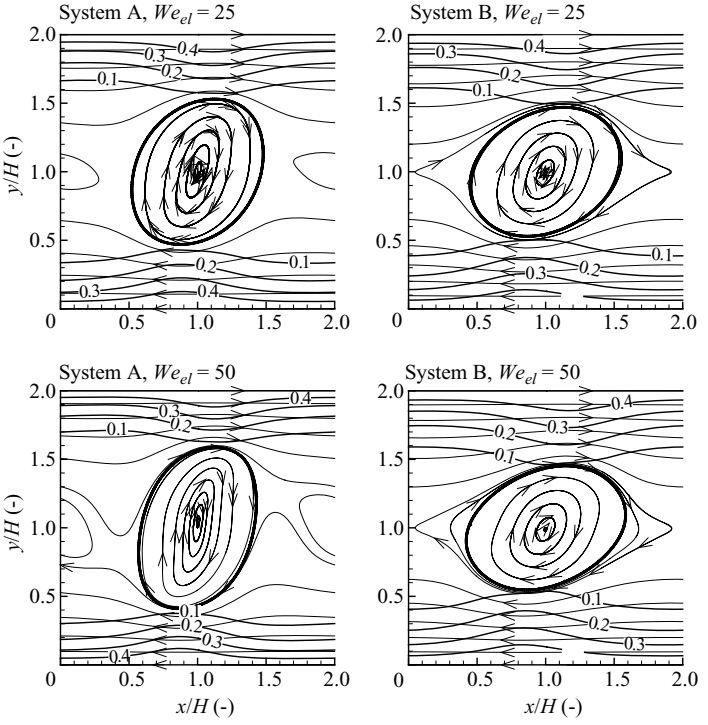

FIGURE 13. Streamline patterns and contours of the kinetic energy of a periodic array of liquid drops in simple shear flow at $Ca = 0.2, 0.4, 0.6, 0.8$, $Re = 1.$ when an electric field at $We_{el} = 25, 50$ is present in the gap. The fluids are leaky dielectrics and represent system A (left panel) and system B (right panel), respectively.

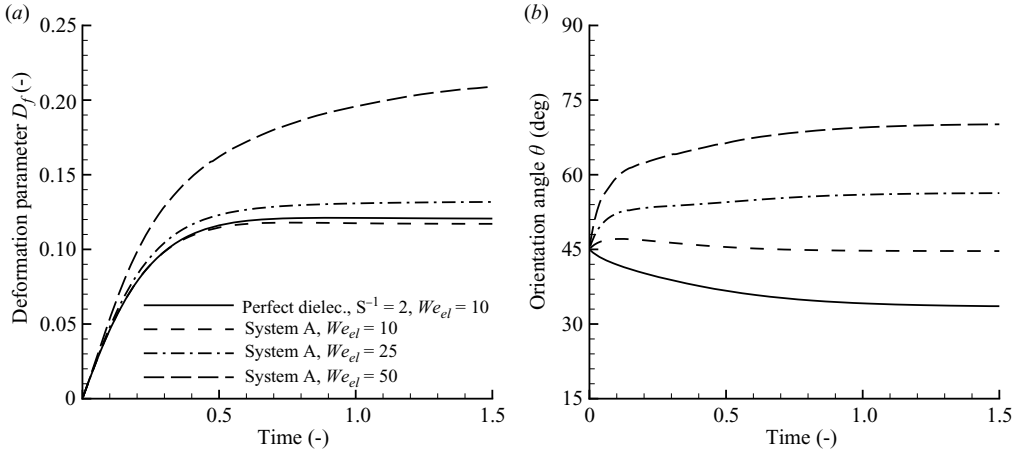

FIGURE 14. Evolution of the deformation parameter D_f of a periodic array of liquid drops suspended in simple shear flow (leaky dielectric system A) at $Ca = 0.2, 0.4, 0.6, 0.8$, $Re = 1$ when an electric field given by $We_{el} = 10, 25, 50$ is present in the gap.

In figure 14 we present a comparison of the leaky dielectric system A with a perfect dielectric system having permittivity ratio $S^{-1} = 2$. Results for the evolution of the deformation parameter D_f and the corresponding orientation angle are shown for a

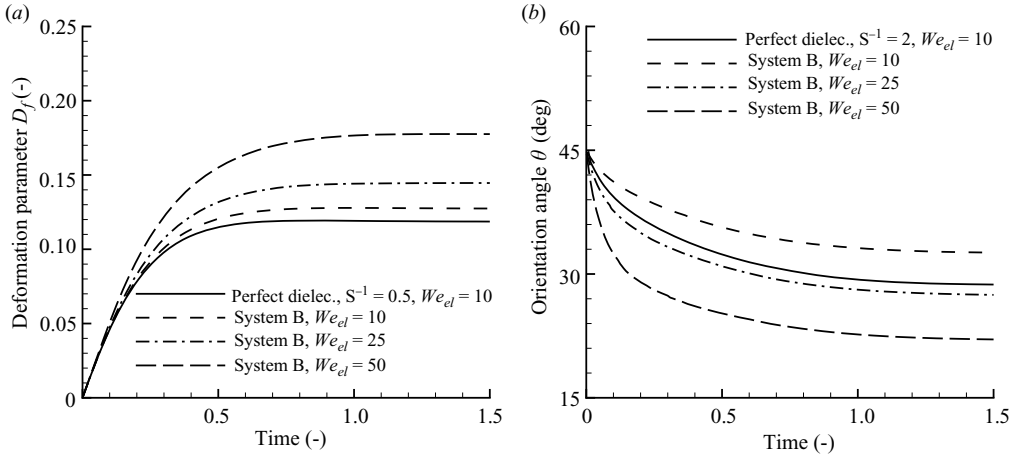

FIGURE 15. Evolution of the deformation parameter D_f of a periodic array of liquid drops suspended in simple shear flow (leaky dielectric system B) at $Ca = 0.2, 0.4, 0.6, 0.8$, $Re = 1$, when an electric field given by $We_{el} = 10, 25, 50$ is present in the gap.

range of values of $We_{el} = 10, 25, 50$. The results reveal that at small electric Weber numbers ($We_{el} = 10$) the drop in system A experiences smaller deformations but larger orientation angles than those in the perfect dielectric system. As We_{el} increases the deformations increase and the drops tend to align with the vertical – the orientation angles satisfy $\theta > 45^\circ$ as found previously in the results of figure 13.

Analogous results for system B are depicted in figure 15 where a comparison with the perfect dielectric case having $S^{-1} = 0.5$ is carried out. The deformation parameter D_f exhibits a monotonic increase with We_{el} with the smallest values achieved by the perfect dielectric system which is electrified with a field strength characterized by $We_{el} = 10$. We can conclude, therefore, that for system B the presence of finite conductivity when the drop to suspension permittivity ratio is less than one tends to enhance the deformation monotonically in contrast to system A which undergoes a reduction in deformation initially until We_{el} increases sufficiently (see figure 14). The main difference between the results for systems A and B are in the orientation angles encountered after a sufficiently long evolution. For system B (see figure 15*b*) the orientation angle increases, relative to the perfect dielectric case, at the smallest electric Weber number $We_{el} = 10$. As We_{el} increases to values of 25 and 50, a monotonic reduction in θ is observed with orientation angles becoming as small as 20°, approximately. This in turn implies that the drop for system B tends to align with the horizontal as We_{el} increases. Our results show that in leaky dielectric systems with relative permittivity $S^{-1} > 1$ the drops can be caused to align with the vertical by increasing the electric field strength. In contrast, for permittivities $S^{-1} < 1$ (system B) an increase in electric field strength tends to align the drops with the horizontal so that the field in this case acts in tandem with the shear and surface tension forces.

5. Conclusions

The effect of an electric field on a periodic suspension of viscous drops in a Couette device has been studied in this article. The numerical approach rests on the classical projection method for the Navier–Stokes equations and the level set technique for the evolution of the fluid–fluid interface. Moreover, the CSF technique is employed

to incorporate the interfacial stresses generated by the curvature and the electric field into the momentum equations as volumetric source terms. The results of the numerically simulated drop deformation due to incident shear have demonstrated that the implemented method of solution is capable of tracking the drop dynamics accurately and the code has been used to explore the effect of electric fields on drop deformation in an underlying shear.

The effect of an electric field on the drop deformation has been simulated for different field intensities and for both perfect as well as leaky dielectric suspensions. It is known from the hydrodynamics literature that drop deformation and elongation takes place as the Reynolds number or capillary number are increased. In the electrohydrodynamic problem we have established two additional ways that deformation and drop extension (possibly indefinite elongation if the parameters are chosen appropriately) take place in perfect dielectric systems. We find that for fixed capillary numbers, Reynolds numbers and electrical properties of the fluids, the effect of an increasing electric field (measured by the dimensionless electric Weber number We_{el}) is to deform the drop into an increasingly elongated shape and at the same time to increase its orientation angle with the horizontal. Therefore, the drop elongates and tends to align vertically with the imposed electric field, but is prevented from doing so by the underlying flow which in turn tends to align the deformed drop with the incident shear direction. The interaction between these mechanisms determines the ultimate configuration and it has been established numerically that steady states which emerge at relatively small capillary numbers, transform to unsteady continuously deforming states at sufficiently large values of We_{el}. As a result of the additional deformation and orientation with the vertical induced by the electric field, the distance between the poles of the drop and the channel walls decreases and modifies the distribution of the pressure and shear stress along the wall.

Variations of the permittivity ratio for perfect dielectric systems have also been considered and in addition to some interesting non-monotonic behaviour in the steady-state deformation parameter as $S^{-1} = \epsilon_2/\epsilon_1$ is increased from small values, we find that the drop can be deformed significantly by increasing S^{-1}, all other parameters kept fixed. The physical reason for this is the decrease of the field inside the droplet when its permittivity is much larger than that of the surrounding fluid, which in turn induces larger values of the Maxwell stresses at the interface. These results are given in figures 10 and 11.

Computations have also been carried out at a Reynolds number $Re = 10$ in order to assess the effect of higher inertia. Values of $Ca = 0.2, 0.4, 0.6, 0.8$ were chosen and the flow computed for $We_{el} = 0$ (no field present) and $We_{el} = 10$. It is established in all cases that the deformation is larger than that for the lower Reynolds number $Re = 1$ and that the orientation angle with the horizontal increases for the larger value of Re. These conclusions can be drawn from the results of figures 7 and 8 and those of figure 12. For example, the deformation for $Ca = 0.2$, $Re = 1$, $We_{el} = 10$ is $D_f \approx 0.12$ whereas for $Ca = 0.2$, $Re = 10$, $We_{el} = 10$ it is $D_f \approx 0.23$, that is almost twice as large. Corresponding results for the orientation angles are $\theta \approx 40^\circ$ for $Re = 1$ and $\theta \approx 70^\circ$ for $Re = 10$, implying a tendency for the alignment of the drop with the vertical as the Reynolds number increases. Similar trends are observed for other values of Ca.

Systems of leaky dielectrics have also been studied and in particular two representative cases have been computed in detail. The first system consists of a drop which is less conducting but having higher permittivity than the surrounding fluid, while for the second system the drop is more conducting but has a lower permittivity than the suspending fluid. These cases are motivated by the drop/suspending fluid

systems of castor oil in silicone oil or vice versa (see §4 and Burcham & Saville 2000 for values). Compared to a base case of perfect dielectric systems having a permittivity ratio $S^{-1}=2$, we find that a drop which is less conducting than the suspending fluid but at the same permittivity ratio ($S^{-1}=2$) deforms more and tends to align with the vertical. The opposite behaviour is found for a more conducting drop but which also has a smaller permittivity than the surrounding medium (in fact $S^{-1}=0.5$ in our computations). That is, the deformation is smaller and the drop is more aligned with the horizontal becoming more oblate than the perfect dielectric case. These conclusions are established from the orientation angle plots included in figure 14(*b*). The change in the orientation towards the vertical brings the drop poles closer to the walls of the Couette device and affects the distribution of pressure and shear stress along the walls. For conducting systems, therefore, our results indicate that an electric field can be used to enhance or reduce deformation and orientation with the vertical relative to the perfect dielectric or indeed non-electrified flow. Such findings may be useful in the design of processes that require the control of drop evolution and final shapes.

We close with some tentative comments regarding the effect of electric fields in the elongation and breakup of drops in three dimensions. It is known that highly viscous three-dimensional drops ($\lambda > 4$) cannot be made to exhibit infinite elongation by increasing the shear rate (we thank a referee for pointing this out). An electric field may be useful in elongating the thread beyond the $\lambda \approx 4$ threshold, by analogy with the present two-dimensional calculations. Regarding capillary instability, the presence of an electric field typically reduces both growth-rates and the band of unstable wavenumbers, enhancing stability. Therefore, one can envision the use of a field for elongation of threads but then switching it off to allow pinch-off in the usual Rayleigh instability scenario.

SM was supported by a research grant from the Deutsche Forschungsgemeinschaft while at NJIT. The work of DTP was supported in part by the National Science Foundation Grants DMS-0072228 and DMS-0707339. Computer time on the parallel cluster of the Department of Mathematical Sciences at NJIT is also greatly acknowledged.

REFERENCES

Adalsteinsson, D. & Sethian, J. 1995 The fast level set method for propagating interfaces. *J. Comp. Phys.* **118**, 269–277.

Adalsteinsson, D. & Sethian, J. 1999 The fast construction of extension velocities in level set methods. *J. Comp. Phys.* **148**, 2–22.

Allan, R. S. & Mason, S. G. 1962 Particle behaviour in shear and electric fields. 1. Deformation and burst of fluid drops. *Proc. R. Soc. Lond. Ser.* A **267**, 45–61.

Brackbill, J. U., Kothe, D. B. & Zemach, C. 1992 A continuum method for modeling surface tension. *J. Comp. Phys.* **100**, 335–354.

Bretherton, F. P. 1961 The motion of long bubbles in tubes. *J. Fluid Mech.* **10**, 166–188.

Burcham, C. L. & Saville, D. A. 2000 The electrohydrodynamic stability of a liquid bridge: microgravity experiments on a bridge suspended in a dielectric gas. *J. Fluid Mech.* **405**, 37–56.

Charles, R. & Pozrikidis, C. 1998 Effect of the dispersed phase viscosity on the simple shear flow of suspensions of liquid drops. *J. Fluid Mech.* **365**, 205–233.

Chopp, D. L. 2001 Some improvements of the fast marching method. *SIAM J. Sci. Comp. (USA)* **23**, 230–244.

Chorin, A. 1968 Numerical solution of the Navier–Stokes equations. *Math. Comput.* **22**, 745–762.

Collins, R. T., Jones, J. J., Harris, M. T. & Basaran, O. A. 2008 Electrohydrodynamic tip streaming and emission of charged drops from liquid cones. *Nature Phys.* **4**, 149–154.

Cristini, V. & Tan, Y.-C. 2004 Theory and numerical simulation of droplet dynamics in complex flows – a review. *Lab Chip* **4**, 257–264.

De Menech, M. 2006 Modeling of droplet breakup in a microfluidic T-shaped junction with a phase-field model. *Phys. Rev.* E **73** (3), 1–9.

Feng, J. Q. 1999 Electrohydrodynamic behaviour of a drop subjected to a steady uniform electric field at finite electric reynolds number. *Proc. R. Soc. Lond.* A **455**, 2245–2269.

Feng, J. Q. 2002 A 2d electrohydrodynamic model for electrorotation of fluid drops. *J. Colloid Interface Sci.* **246**, 112–121.

Feng, J. Q. & Scott, T. C. 1996 A computational analysis of electrohydrodynamics of a leaky dielectric drop in an electric field. *J. Fluid Mech.* **311**, 289–326.

Fernández, A., Tryggvason, G., Che, J. & Ceccio, S. L. 2005 The effects of electrostatic forces on the distribution of drops in a channel flow: two-dimensional oblate drops. *Phys. Fluids* **17** (9), 1–15.

Kennedy, M. R., Pozrikidis, C. & Skalak, R. 1994 Motion and deformation of liquid drops, and the rheology of dilute emulsions in simple shear flow. *Comp. Fluids* **23**, 251–278.

Khismatulin, D., Renardy, Y. & Cristini, V. 2003 Inertia-induced breakup of highly viscous drops subjected to simple shear. *Phys. Fluids* **15**, 1351–1354.

Lac, E. & Homsy, G. M. 2007 Axisymmetric deformation and stability of a viscous drop in a steady electric field. *J. Fluid Mech.* **590**, 239–264.

Lee, J. & Pozrikidis, C. 2006 Effect of surfactants on the deformation of drops and bubbles in Navier–Stokes flow. *Comp. Fluids* **35** (1), 43–60.

Li, X., Charles, R. & Pozrikidis, C. 1996 Simple shear flow of suspensions of liquid drops. *J. Fluid Mech.* **320**, 395–416.

Li, J., Renardy, Y. & Renardy, M. 2000 Numerical simulation of breakup of a viscous drop in simple shear flow through a volume-of-fluid method. *Phys. Fluids* **12**, 269–282.

Li, X., Zhou, H. & Pozrikidis, C. 1995 Numerical study of the shearing motion of emulsions and foams. *J. Fluid Mech.* **286**, 379–404.

Melcher, J. R. & Taylor, G. I. 1969 Electrohydrodynamics: a review of the role of interfacial shear stresses. *Annu. Rev. Fluid Mech.* **1**, 111–146.

O'Konski, C. T. & Thacher, H. C. Jr. 1953 The distortion of aerosol droplets by an electric field. *J. Phys. Chem.* **57**, 955–958.

Osher, S. & Sethian, J. 1988 Front propagating with curvature dependent speed: algorithms based on Hamilton–Jacobi formulations. *J. Comp. Phys.* **79**, 12–49.

Osher, S. & Shu, C.-W. 1991 High order essentially non-oscillatory schemes for Hamilton Jacobi equations. *SIAM J. Num. Anal.* **28**, 907–922.

Ozen, O., Aubry, N., Papageorgiou, D. T. & Petropoulos, P. G. 2006 Monodisperse drop formation in square microchannels. *Phys. Rev. Lett.* **96**, Art. 144501.

Peskin, C. S. 1977 Numerical analysis of blood flow in the heart. *J. Comp. Phys.* **25**, 220–252.

Pozrikidis, C. 1997 Numerical studies of singularity formation at free surfaces and fluid interfaces in two-dimensional Stokes flow. *J. Fluid Mech.* **331**, 145–167.

Pozrikidis, C. 1998 Numerical studies of cusp formation at fluid interfaces in Stokes flow. *J. Fluid Mech.* **357**, 29–57.

Rallison, J. M. 1981 A numerical study of the deformation and burst of a viscous drop in general shear flows. *J. Fluid Mech.* **109**, 465–482.

Rallison, J. M. & Acrivos, A. 1978 A numerical study of the deformation and burst of a viscous drop in an extensional flow. *J. Fluid Mech.* **89**, 191–200.

Renardy, Y. 2007 The effects of confinement and inertia on the production of droplets. *Rheol. Acta* **46**, 521–529.

Renardy, Y. & Cristini, V. 2001 Scalings for fragments produced from drop breakup in shear flow with inertia. *Phys. Fluids* **13**, 2161–2164.

Rhodes, P. H., Snyder, R. S. & Roberts, G. O. 1989 Electrohydrodynamic distortion of sample streams in continuous flow electrophoresis. *J. Colloid Interface Sci.* **129**, 78–90.

Ryskin, G. & Leal, L. G. 1984 Numerical solution of free-boundary problems in fluid mechanics. Part 3. Bubble deformation in an axisymmetric straining flow. *J. Fluid Mech.* **148**, 37–43.

Saville, D. A. 1997 Electrohydrodynamics: the Taylor–Melcher leaky dielectric model. *Annu. Rev. Fluid Mech.* **29**, 27–64.

Sethian, J. 1996 A fast marching level set method for monotonically advancing fronts. *Proc. Acad. Nat. Sci.* **93**, 1591–1595.

Sethian, J. 1999 Fast marching methods. *SIAM Rev.* **41**, 199–235.

Shankar, V. & Sharma, A 2004 Instability on the interface between thin fluid films subjected to electric fields. *J. Colloid Interface Sci.* **274**, 294–308.

Sheth, K. & Pozrikidis, C. 1995 Effects of inertia on the deformation of liquid drops in simple shear flow. *Comp. Fluids* **24** (2), 101–119.

Sibillo, V., Pasquariello, G., Simeone, M., Cristini, V. & Guido, S. 2006 Drop deformation in microconfined shear flow. *Phys. Rev. Lett.* **97**, 0545021–0545024.

Smith, C. V. & Melcher, J. R. 1967 Electrohydrodynamically induced spatially periodic cellular Stokes-flow. *Phys. Fluids* **10**, 2315–2322.

Song, H., Chen, D. L. & Ismagilov, R. F. 2006 Reactions in droplets in microfluidic channels. *Angewandte Chemie – International Edition* **45** (44), 7336–7356.

Stone, H. A. 1994 Dynamics of drop deformation and breakup in viscous fluids. *Annu. Rev. Fluid Mech.* **26** (1), 65–102.

Stone, H. A., Stroock, A. D. & Ajdari, A. 2004 Engineering flows in small devices: microfluidics toward a lab-on-a-chip. *Annu. Rev. Fluid Mech.* **36**, 381–411.

Sussman, M. & Fatemi, E. 1999 An efficient interface-preserving level set redistancing algorithm and its application to interfacial incompressible fluid flow. *SIAM J. Sci. Comp.* **20**, 1165–1191.

Sussman, M., Fatemi, E., Smereka, P. & Osher, S. 1994 A level set approach for computing solutions to incompressible two-phase flows. *J. Comp. Phys.* **100**, 146–159.

Taylor, G. I. 1934 The formation of emulsions in definable fields of flow. *Proc. R. Soc. Lond.* **146**, 501–523.

Taylor, G. I. 1966 Studies in electrohydrodynamics: I. The circulation produced in a drop by an electric field. *Proc. R. Soc. Lond. Ser.* A **291**, 159–166.

Tomar, G., Gerlach, D., Biswas, G., Alleborn, N., Sharma, A., Durst, F., Welch, S. W. J. & Delgado, A. 2007 Two-phase electrohydrodynamic simulations using a volume of fluid approach. *J. Comp. Phys.* **227**, 1267–1285.

Unverdi, O. & Tryggvason, G. 1992 A front-tracking method for viscous incompressible, multi-fluid flows. *J. Comp. Phys.* **100**, 25–37.

Wagner, A. J., Wilson, L. M. & Cates, M. E. 2003 Role of inertia in two-dimensional deformation and breakdown of a droplet. *Phys. Rev.* E **68**, 453011–453014.

Ward, T. & Homsy, G. M. 2001 Electrohydrodynamically driven chaotic mixing in a translating drop. *Phys. Fluids* **13**, 3521–3525.

Ward, T. & Homsy, G. M. 2003 Electrohydrodynamically driven chaotic mixing in a translating drop. II. Experiments. *Phys. Fluids* **15**, 2987–2994.

Zhou, H. & Pozrikidis, C. 1993*a* The flow of suspensions in channels: single files of drops. *Phys. Fluids* A **5**, 311–323.

Zhou, H. & Pozrikidis, C. 1993*b* The flow of ordered and random suspensions of two-dimensional drops in a channel. *J. Fluid Mech.* **255**, 103–127.

Zhou, H. & Pozrikidis, C. 1994 Pressure-driven flow of suspensions of liquid drops. *Phys. Fluids* **6**, 80–94.